Imaging Unstained Synthetic Polymer Crystals and Defects on Atomic Length-scales using Cryogenic Electron Microscopy

Xi Jiang[1], Douglas R. Greer[1,2], Joyjit Kundu[3,4], Colin Ophus[3], Andrew M. Minor[3,5], David Prendergast[3], Ronald N. Zuckermann[3], Nitash P. Balsara[1,2], Kenneth H. Downing[6]**

[1] Materials Sciences Division, Lawrence Berkeley National Laboratory, Berkeley, CA 94720 United States.

[2] College of Chemistry, University of California, Berkeley, Berkeley, CA 94720 United States.

[3] Molecular Foundry, Lawrence Berkeley National Laboratory, Berkeley, CA 94720 United States.

[4] Department of Chemistry, Duke University, Durham, North Carolina 27708 United States.

[5] Department of Materials Science & Engineering, University of California, Berkeley, Berkeley, CA 94720 United States.

[6] Molecular Biophysics and Integrated Bioimaging Division, Lawrence Berkeley National Laboratory, Berkeley, CA 94720 United States.

KEYWORDS: peptoids, structure, cryo-EM, polymers, defects

ABSTRACT: Properties of soft crystalline materials such as synthetic polymers are governed by locations of constituent atoms. Determining atomic-scale structures in these materials is difficult because they degrade rapidly when studied by electron microscopy, and techniques such as x-ray scattering average over volumes much larger than coherent blocks of the unit cells. We obtained cryo-electron microscopy images of self-assembled nanosheets of a peptoid polymer, made by solid-phase synthesis, in which we see a variety of crystalline motifs. A combination of crystallographic and single particle methods, developed for cryo-electron microscopy of biological macromolecules, was used to obtain high resolution images of the crystals. Individual crystals contain grains that are mirror images of each other with concomitant grain boundaries. We have used molecular dynamic simulations to build an atomic model of the crystal structure to facilitate the interpretation of electron micrographs. Direct visualization of crystalline

grains and grain boundaries on atomic length scales represents a new level of information for the polymer field.

INTRODUCTION

Crystalline polymers comprise lamellar domains with numerous defects and trapped amorphous domains between and possibly within lamellae. In landmark studies dating back to 1938[1], electron diffraction was used to study thin, single crystal lamellae grown from solution [2-5]. Considerable knowledge on polymer crystals has been obtained by using electron crystallography[6-9] and electron microscopy imaging[10-17] in following decades. Nevertheless, the challenge of imaging polymer crystals in position space remains unaddressed: all images of atoms in the literature on synthetic polymers are drawn either by hand or by computer programs. Here we present electron micrographs of synthetic polymer crystals and defects that can be interpreted in terms of simulated atomic models.

Electron microscopy is routinely used to image two classes of materials with Angstrom level resolution: hard crystalline materials such as metals and biological macromolecules such as proteins. Many metals are stable to electron beam exposure, which makes it possible to obtain images under high dose conditions in which individual atoms are resolved. Proteins, on the other hand, are unstable to electron beam exposure, and determining high resolution structures requires the application of sophisticated data analysis algorithms on numerous images that each have low signal-to-noise ratio

because they are obtained under low dose conditions. The algorithms exploit the fact that in a given sample, the protein molecules have the same atomic structure (or a limited set of structures), even though the images represent projections of that structure through unknown rotations. Crystals of synthetic polymers are also unstable to electron beam exposure. Since the degree of homogeneity at the atomic level in synthetic polymer crystals is generally quite limited, the methods used to solve protein structures cannot be directly applied.

When atomic scale resolution of radiation sensitive soft materials is desired, it is of great importance to minimize the damage from the electron beam. In order to preserve the high spatial frequency signal, the accumulated dose that can be used for imaging has to be carefully controlled by using a low-dose imaging technique. In addition, the effects of radiation damage are minimized when the specimen is cooled to cryogenic temperatures [18, 19]. The resolution of structures obtained from radiation-sensitive biological macromolecules using cryogenic electron microscopy (cryo-EM) has been significantly improved with the introduction of direct electron detectors and novel image processing algorithms [20-23]. The high detective quantum efficiency (DQE) of these detectors and their ability to acquire images rapidly enable dose-fractionated movie recording and beam-induced motion correction, thereby providing substantial enhancement of resolution for low-dose imaging [20, 24, 25]. In the present study, we have leveraged these advances along with algorithms developed in the structural

biology community to obtain images of vitrified, hydrated synthetic polymer crystals using cryo-EM at a resolution sufficient to enable direct comparisons with atomic models.

EXPERIMENTAL SECTION

Diblock polypeptoid synthesis

The amine submonomers for Nte (mPEG3-NH2) were purchased from Peptide Solutions, Inc. (98% purity). Linear alkyl amines were purchased from TCI. All submonomers were used without further purification. Automated solid-phase submonomer synthesis of the polypeptoids was performed on a Symphony X peptide synthesizer at a scale of 200 mg Rink amide resin (0.64 mmol/g) following published procedures (1). Displacement reactions were performed at amine concentrations of 1 M in N,N’-dimethylformamide (DMF) for 30 min at room temperature. Bromoacetylation reactions were performed with bromoacetic acid and N,N'-diisopropylcarbodiimide (both at 0.8 M in DMF) for 20 min at room temperature.

Peptoids were cleaved from resin by treating with an acid cleavage cocktail of dichloromethane/trifluoroacetic acid/water (50/45/5, v/v) for 10 min at room temperature. After resin filtration and washing, the cocktail was evaporated, and the peptoids were lyophilized from acetonitrile/water (1:1, v/v).

Acetylation was performed on the crude, cleaved peptoid (~200 mg). The peptoid was dissolved in 2 mL DMF/tetrahydrofuran (THF) (1:5, v/v), followed

by the addition of 100 µL acetic anhydride and 100 µL pyridine, and allowed to stir at room temperature for 20 minutes. The volatiles were then removed by evaporation, and the peptoid lyophilized from acetonitrile (ACN)/water (1:1, v/v).

Purification and self-assembly

Purification was performed on a reverse phase HPLC Waters prep system using a XSelect HSS cyano column (5 µm, 18 x 150 mm). A linear, binary elution gradient was used (where solvent A was 10% isopropyl alcohol (IPA) in water, and solvent B was 10% IPA in ACN), from 50 – 95% B in 20 minutes at a flow rate of 20 mL/min). Note that TFA was not included in the buffer system, since the peptoid N-acetyl group exhibits some acid lability. 50 mg of peptoid dissolved in 3 mL of ACN/water (1:1, v/v) was used per injection. The fractions were collected and analyzed by MALDI using a superDHB matrix. The collected fractions containing pure product were combined, evaporated, and lyophilized from ACN/water (1:1, v/v) to afford a fluffy white powder. The product was then analyzed by reverse phase HPLC equipped with an analytical cyano column and MicroTOF electrospray mass spectrometer. 50 mg of final product was obtained in 90% purity. Analysis of molecular purity is provided in Figure S1.

To form the nanosheets, the polymers were dissolved in THF/water (1:1, v/v) at a concentration of 2 mg/mL. The THF was removed by slow evaporation under a vacuum of 500 Torr at room temperature, over a period

of 24 hours. The solution turned turbid, indicating the formation of aggregates.

EM data collection

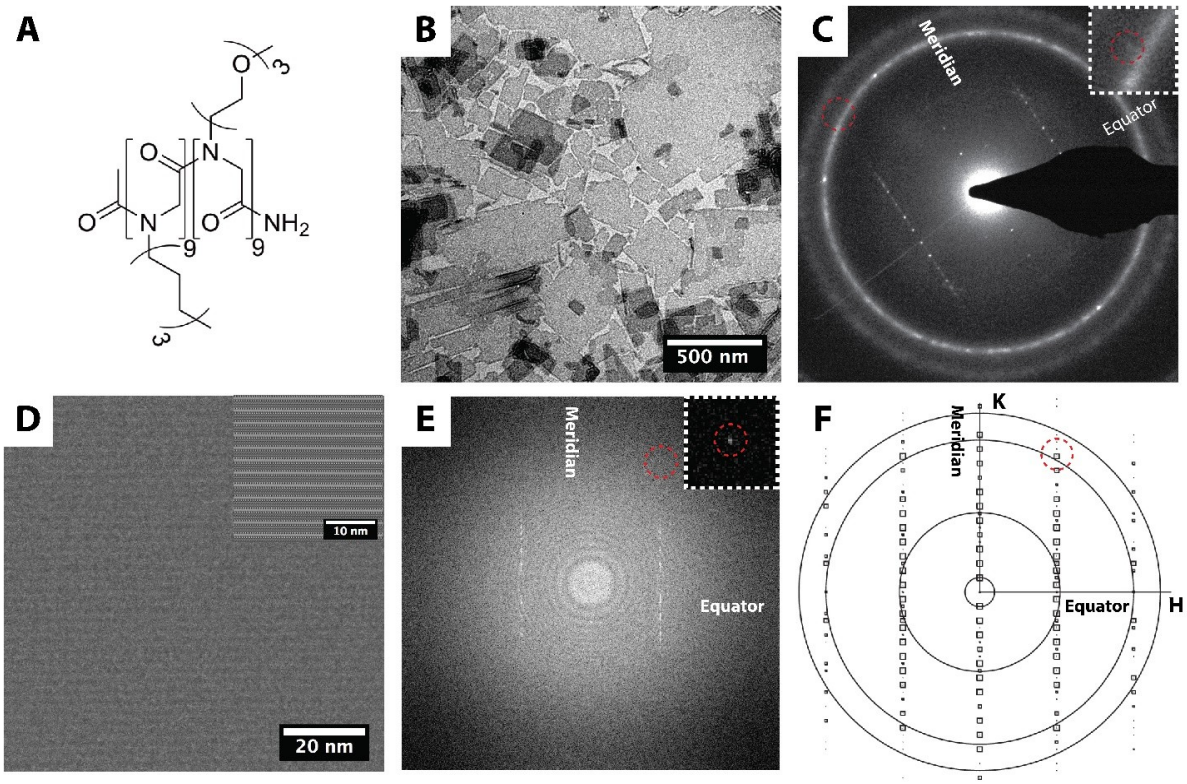

Figure 1. Chemical structure and EM characterization. A, Chemical structure of peptoid $pNdc_9$–$pNte_9$. **B**, TEM micrograph of $pNdc_9$–$pNte_9$ sheets. **C**, Cryogenic electron diffraction pattern of a vitrified hydrated $pNdc_9$–$pNte_9$ sheet; the brighter ring corresponds to gold 111 diffraction at 2.35Å, inset red circle indicates (1, 19) reflection at 2.3 Å. **D**, Cryo-EM micrograph (reversed contrast) of a vitrified hydrated $pNdc_9$–$pNte_9$ sheet; inset shows a Fourier filtered image. **E**, The Fourier transform of an image of a vitrified

hydrated $pNdc_9$–$pNte_9$ sheet showing reflections and Thon rings due to the thin carbon support; red circle in inset indicates the (1, 19) reflection. **F**, Information in Fourier transform of image after correction for lattice distortions. The rings represent resolution of 2.0, 2.35, 4.5, and 24.5 Å, H and K indicate directions of lattice vectors, and red circle indicates the (1, 19) reflection. The squares indicate the signal-to-noise ratio of reflections: the larger the square is, the better the image quality (IQ) [26].

All of the analysis of atomic-scale micrograph in this paper were obtained from unstained, vitrified, hydrated nanosheets that were prepared for low-dose cryo-EM experiments on C-Flat grids (Protochips Inc.), covered by a thin, continuous carbon film (10 nm), using a Vitrobot (FEI Inc.). The specimens were imaged with a Titan Krios (FEI Inc.) operated at 300 kV with K2 Summit direct detection camera (Gatan Inc.) using defocus values from -1.0 to -0.5 µm. Dose-fractionation movies comprising 20 frames were recorded using the super-resolution setting on the camera. This setting extends the Nyquist frequency range of the micrograph[20, 27]. The accumulated dose for each movie was 20 e/Å^2. Movie frames were aligned and summed by MotionCorr2[24] to eliminate beam-induced motion. Low-dose electron diffraction patterns were collected on vitrified hydrated nanosheets prepared on C-Flat grids with pre-deposited gold crystals. The specimen was transferred to a TEM cryo holder (914 Gatan Inc.) and electron diffraction patterns were collected on a Philips CM-200 at 200 kV with camera length of 1000 mm, using a Gatan Ultrascan CCD camera. The specimen area

illuminated by the electron beam was about 1 μm diameter. Low resolution micrographs were obtained from stained, air-dried nanosheets that were prepared by mixing a 2% wt/vol aqueous solution of uranyl acetate with nanosheets in aqueous suspension. A 3 μl droplet was deposited on continuous carbon film on a copper grid and blotted using filter paper from the edge of the grid. TEM micrographs were obtained using a Philips CM200 at 200 kV.

RESULTS AND DISCUSSION

The polymer used in this study is a nearly monodisperse short diblock polypeptoid comprising a hydrophobic poly-*N*-decylglycine (pNdc) block and a hydrophilic poly-*N*-2-(2-(2-methoxyethoxy) ethylglycine) (pNte) block. This class of diblock copolymers is known to form ordered lamellae in the solid-state and monolayer nanosheets in water [28]. The polymer used in this study, $pNdc_9$-$pNte_9$, shown in Figure 1A, was prepared by automated solid-phase synthesis and purified to >90% molecular purity by HPLC as previously described [28]. Details of synthesis and characterization are given in the Supplementary Information. The polydispersity index for this polymer is 1.00002. The absence of hydrogen bonding, chirality, and electrostatic interactions in these polypeptoids, and their ability to spontaneously assemble into water soluble, crystalline, monolayer nanosheets make them excellent models of synthetic polymers such as polyethylene. The pNdc block forms the crystalline, hydrophobic core of the nanosheet, and the pNte

block is amorphous and solvated by water. The homogeneity of peptoid crystals is expected to be far higher than that of most other polymer crystals such as polyethylene, due to the low polydispersity of the peptoid chains. These monolayer lamellae were formed in high yield and readily imaged by transmission electron microscopy as shown in Figure 1B. The uniform thickness, straight edges and rectangular form of the lamellae indicate substantial crystalline order.

We performed low-dose cryogenic electron diffraction on individual hydrated sheets. The samples were prepared with methods in common use in cryo-EM of proteins, by placing the solution on a copper grid with a pre-deposited holey film and plunging it into liquid ethane (-180 °C). The resulting electron diffraction patterns, such as that shown in Figure 1C, represent Bragg reflections of the pNdc crystals. The diffraction patterns display a prominent 25 Å repeat along the meridian, which has been shown to arise from the spacing of adjacent rows of backbones [28]. In addition, diffraction spots extend along rows parallel to this meridian from a distance corresponding to 4.7 Å. The outermost visible spots are just outside the gold 111 diffraction ring (inset in Figure 1C) and they represent information at 2.3 Å.

We also recorded images of these specimens that yielded information to at least as high resolution. A section of a typical low-dose cryo-EM micrograph is shown in Figure 1D. The bright horizontal lines represent the backbones of the polymer, but the signal-to-noise ratio is so low that little other detail is

detected. However, the Fourier transform of an image including an area 300x300 nm (Figure 1E) shows the presence of strong signal along the 4.7 Å rows. The appearance of weak diffraction between some of the stronger spots along these rows, along with the absence of intensity on these rows at 90 degrees from the meridian, suggested the presence of a glide plane, and the diffraction patterns were indexed with plane group P121 with a=4.7 Å, b=50 Å. Streaking of some of the spots suggests some degree of disorder in the crystals. The CTF estimation of FFT in Figure 1E can be found in Fig. S2 in SI.

We applied the crystallographic processing that has been developed in the context of cryo-EM of monolayer protein crystals to further analyze the images [26]. The 2dx software package was used to identify and correct lattice distortions in the image as well as to correct for the contrast transfer function (CTF) of the microscope [29, 30]. Following this unbending step, reflections that are not evident in the electron diffraction pattern can be detected with good signal-to-noise ratio, even beyond 2 Å. A representation of the data from one micrograph is shown in Figure 1F and Supplementary Fig. S2.

We used 2dx to analyze images of 12 independent, nominally untilted crystalline nanosheets of the type depicted in Figure 1. Most of these yielded unit cell maps with higher than expected symmetry (see Supplementary Figure S3), suggesting an artifact in the processing. We thus

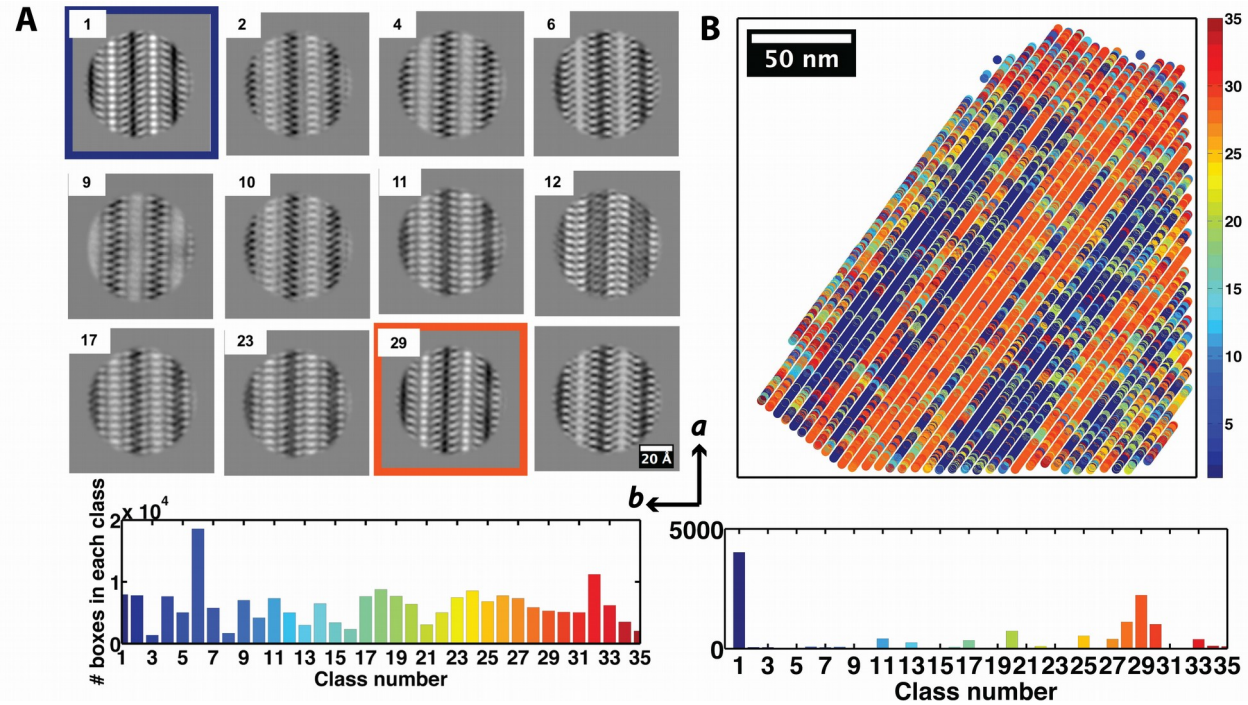

Figure 2. Structural variations of crystals and distribution map. A, 12 dominant classes from 35 classes found in a set of 12 micrographs of nominally untilted specimens. Histogram below shows the population of each of the 35 classes. **B**, Distribution of classes in one micrograph. The two major classes, 1 and 29, are mirror images of each other. Histogram below shows the population of classes in this image.

applied a tool developed in the context of cryo-EM of macromolecular complexes to study this effect by identifying a set of characteristic unit cell images. We extracted boxes of 87 x 87Å at the locations of each unit cell, which were determined during the unbending step as shown in Fig. S4. These boxes were sorted into 35 classes and averaged using the Relion software package [23]. The twelve most highly populated classes are shown in Figure 2A. Images of all 35 class averages are shown in Supplementary

Figure S5, along with the Fourier transforms of each class average in Supplementary Figure S6. Most of these images show two anti-parallel sets of closely packed V-shaped motifs with a bright feature running through the vertices. Mapping the locations within the original micrographs of each class member revealed not only that each micrograph contained predominantly a small subset of the classes, but that there was frequently a domain structure within the crystals. Figure 2B shows, for one of the micrographs, the locations of unit cells belonging to the various classes, along with a histogram of the class membership within the image. This micrograph is dominated by two motifs, corresponding to classes 1 and 29 (29 and 31 are nearly identical as shown in Supplementary Figure S5). These motifs are mirror images and are clustered into welldefined domains. Boundaries between domains containing the two motifs run along the closepacked rows, generally spanning the entire crystal. Analysis of more of the images is shown in Supplementary Figure S7. The set of class average images contains several near duplicates and pairs that are mirror images. They can be sorted into 8 main groups, as shown in Supplementary Figure S5. Common features of all of the images include a bright line running along the apex of a V-shaped structure with arms extending symmetrically out on both sides of this line. The spacing between the lines is consistently 25 Å and between the arms 4.7 Å. Differences in the width of the line and contrast of a 4.7 Å spacing along it define the different groups. Visual examination of class averages 1 and 29 (Figure 2A) suggests that they represent the

sidechains extending from peptoid backbones which run perpendicular to the plane of the lamellae.

A molecularly thin sheet of peptoid crystal with this structure is shown schematically in Figure 3A where we focus on the hydrophobic pNdc$_9$ crystal. The sheet is stabilized by hydrophilic pNte9 chains that extend into the surrounding water (shown in atomic models in Supplementary Figure S8). Also shown in Figure 3B are the in-plane and through-plane views

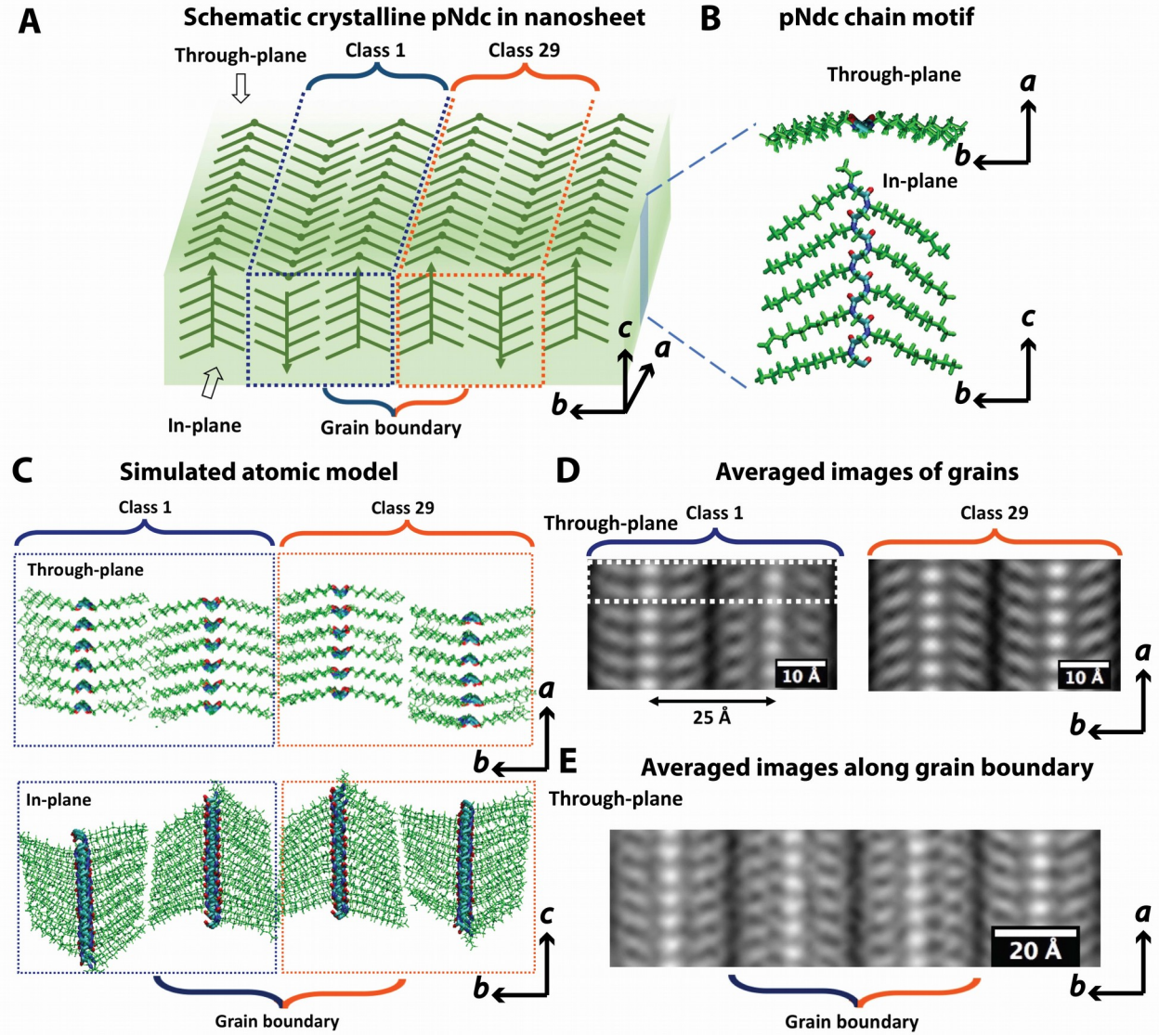

Figure 3. Model and imaging of individual crystals and grain boundaries. **A,** Cartoon shows overall arrangement of pNdc chains in a crystallized nanosheet showing anti-parallel arrangement of adjacent molecules within a crystal and a grain boundary between two crystals. **B,** Typical conformation of a pNdc block obtained by simulations showing through-plane ("top") and in-plane ("front") views as indicated. The V-shaped motif arises due to the cis backbone conformation. Nitrogen atoms

are blue, oxygen red, carbon cyan in backbones (see Supplementary Information for details). **C**, Region extracted from relaxed computer simulation of crystal that includes a grain boundary, with regions marked corresponding to images in class averages 1 and 29. **D**, Averaged images obtained by sorting unit cells in the micrograph of Figure 2 into six classes. The most highly populated classes from this sorting correspond to classes 1 and 29 of Figure 2. **E**, An image obtained by averaging boxes along the domain boundaries in the micrograph of Figure 2 matches the model structure at the boundary.

of a typical $pNdc_9$ chain in the crystal obtained using molecular dynamic simulations described in SI (see Figure S8 and PDB files). Models of $pNdc_9$-$pNte_9$ peptoid chains in several monolayer crystalline arrangements in water were allowed to relax using molecular dynamics. The backbones stayed roughly parallel to each other and the pNdc sidechains maintain the ordered V-shaped motifs that exclude water, while the pNte sidechains extend into solution and are disordered. Simulations of models with or without grain boundaries showed no detectable energy penalty for the defect. Figure 3C shows in-plane and through-plane views of a section of a simulated pNdc crystalline sheet. The simulation results closely resemble the averaged images of class 1 and class 29.

Figure 3D shows the experimentally obtained micrographs for class averages 1 and 29. The correspondence between these micrographs and

the through-plane views of our model (Figure 2B) is clear. The average distances between adjacent backbones and sidechains are 25 Å and 4.7 Å in the model, in agreement with the spacings in the images. Grain boundaries are frequently observed in these crystals; see boundaries between red and blue spots in Figure 2B. Averaging unit cells along such grain boundaries results in the image shown in Figure 3E. Here we obtain two adjacent V-shaped motifs that are parallel to each other in the middle of the micrograph, representing a grain boundary between class averages 1 and 29. This is in sharp contrast to the interior of grains that exhibit chains with two anti-parallel sets V-shaped motifs. The image of the defect is more noisy due to the fact that there are relatively few boxes located at the 1/29 boundary. The agreement between the simulated atomic model presented in Figure 3C and the micrographs in Figure 3D demonstrates the ability of our approach to identify both crystalline arrangements as well as individual defects. In addition, the micrographs show the presence of a 4.5 A gap between adjacent molecules, consistent with through-plane projections of simulations

The molecular motifs underlying the other image classes that we observe have yet to be identified, although the similarities in spacings suggest that they are all views essentially down the backbones. It seems unlikely that they represent simply different orientations of the crystal, since we find no correlation between the image patterns and specimen tilt angles determined in the course of the crystallographic processing. Our work only represents

the beginning of characterizing synthetic polymer crystals at the atomic scale.

CONCLUSIONS

In conclusion, we have obtained low-dose electron micrographs of synthetic polypeptoid crystals at around 2 Å resolution. A challenging aspect of the data from these synthetic polymer crystals was the apparent presence of numerous distinct crystalline motifs in a contiguous film. In order to deal with this issue, micrographs were divided into small blocks of unit cells which were then classified and averaged, using techniques developed by the structural biology community. This sorting suggested diverse chain conformations and unit cell packing arrangements within the crystals. Molecular simulations were used to identify some of the stable arrangements that are consistent with the imaging results, with good correspondence between proposed atomic models and observed motifs. It is evident that polymer chains can be trapped in periodic motifs that are out-of-equilibrium; direct imaging on atomic length scales is essential for identifying these motifs. Samples were often composed of contiguous regions with motifs that were mirror images of each other. By analyzing the boundaries of these regions, we were able to image crystalline defects. The present study is the first to demonstrate the possibility of atomic-scale imaging of synthetic polymer crystals and concomitant defects. The approach developed is robust and can, in principle, be applied to other synthetic polymer crystals

provided the samples contain sufficient numbers of crystalline motifs to allow the hybrid analysis using crystallographic and single particle methods. The work in this paper is restricted to short polymer chains that do not fold within the crystal. Atomic scale imaging of crystals with folded chains will present additional challenges that we hope to address in future work.

ASSOCIATED CONTENT

Supporting Information

Imaging processing and molecular dynamics simulation

References

Figures S1-S8

Caption for atomic models

Atomic models in PDB format

AUTHOR INFORMATION

Corresponding Author

* Correspondence to: khdowning@lbl.gov (K.H.D), nbalsara@berkeley.edu (N.P.B)

FUNDING SOURCES

Funding for this work was provided by the Soft Matter Electron Microscopy Program (KC11BN), supported by the Office of Science, Office of Basic Energy Science, US De-partment of Energy, under Contract DE-AC02-05CH11231. Portions of cryo-EM data collection in the present study were carried out with facilities supported by NIH grant GM51487 and at the Krios microscopy facility, University of California Berkeley, supported by the Bay Area Cryo-EM Consortium.

NOTES

The authors declare no competing financial interest.

ACKNOWLEDGMENTS

We gratefully acknowledge Dr. Robert M. Glaeser and Dr. Bong Gyoon Han for many discussions and Dr. Ryan Spencer, Dr. Stephen Whitelam and Dr. John R. Edison for help with molecular model building.

REFERENCES

1. Storks, K. H. An electron diffraction examination of some linear high polymers. *J Am Chem Soc* **1938,** 60, 1753-1761 DOI: DOI 10.1021/ja01275a013.
2. Fischer, E. W. Stufenformiges Und Spiralformiges Kristallwachstum Bei Hochpolymeren. *Z Naturforsch Pt A* **1957,** 12 (9), 753-754.
3. Keller, A. A Note on Single Crystals in Polymers - Evidence for a Folded Chain Configuration. *Philos Mag* **1957,** 2 (21), 1171-& DOI: Doi 10.1080/14786435708242746.
4. Keller, A.; Oconnor, A. Large Periods in Polyethylene - Origin of Low-Angle X-Ray Scattering. *Nature* **1957,** 180 (4597), 1289-1290 DOI: DOI 10.1038/1801289a0.
5. Till, P. H. The Growth of Single Crystals of Linear Polyethylene. *J Polym Sci* **1957,** 24 (106), 301-306 DOI: DOI 10.1002/pol.1957.1202410616.

6. Moss, B.; Dorset, D. L.; Wittmann, J. C.; Lotz, B. Electron Crystallography of Epitaxially Grown Paraffin. *J Polym Sci Pol Phys* **1984,** 22 (11), 1919-1929 DOI: DOI 10.1002/pol.1984.180221106.
7. Dorset, D. L. Crystal-Structure of Lamellar Paraffin Eutectics. *Macromolecules* **1986,** 19 (12), 2965-2973 DOI: DOI 10.1021/ma00166a015.
8. Dorset, D. L. Direct Structure-Analysis of a Paraffin Solid-Solution. *P Natl Acad Sci USA* **1990,** 87 (21), 8541-8544 DOI: DOI 10.1073/pnas.87.21.8541.
9. Dorset, D. L.; Zemlin, F. Direct Phase Determination in Electron Crystallography - the Crystal-Structure of an Normal-Paraffin. *Ultramicroscopy* **1990,** 33 (4), 227-236 DOI: Doi 10.1016/0304-3991(90)90040-S.
10. Dawson, I. M.; Vand, V. Observation of Spiral Growth-Steps in Normal-Paraffin Single Crystals in the Electron Microscope. *Nature* **1951,** 167 (4247), 476-476 DOI: DOI 10.1038/167476a0.
11. Giorgio, S.; Kern, R. High-Resolution Electron-Microscopy of Polyethylene and Paraffin Crystals - Stability in the Electron-Beam. *J Polym Sci Pol Phys* **1984,** 22 (11), 1931-1951 DOI: DOI 10.1002/pol.1984.180221107.
12. Glaeser, R. M.; McMullan, G.; Faruqi, A. R.; Henderson, R. Images of paraffin monolayer crystals with perfect contrast: Minimization of beam-induced specimen motion. *Ultramicroscopy* **2011,** 111 (2), 90-100 DOI: 10.1016/j.ultramic.2010.10.010.
13. Tsuji, M.; Isoda, S.; Ohara, M.; Kawaguchi, A.; Katayama, K. Direct Imaging of Molecular Chains in a Poly(Para-Xylylene) Single-Crystal. *Polymer* **1982,** 23 (11), 1568-1574 DOI: Doi 10.1016/0032-3861(82)90173-2.
14. Revol, J. F.; Manley, R. S. Lattice Imaging in Polyethylene Single-Crystals. *J Mater Sci Lett* **1986,** 5 (3), 249-251 DOI: Doi 10.1007/Bf01748066.
15. Pradere, P.; Thomas, E. L. Image-Processing of Partially Periodic Lattice Images of Polymers - the Study of Crystal Defects. *Ultramicroscopy* **1990,** 32 (2), 149-168 DOI: Doi 10.1016/0304-3991(90)90033-I.
16. Dobb, M. G.; Hindeleh, A. M.; Johnson, D. J.; Saville, B. P. Lattice Resolution in an Electron-Beam Sensitive Polymer. *Nature* **1975,** 253 (5488), 189-190 DOI: DOI 10.1038/253189a0.
17. Martin, D. C.; Thomas, E. L. Experimental High-Resolution Electron-Microscopy of Polymers. *Polymer* **1995,** 36 (9), 1743-1759 DOI: Doi 10.1016/0032-3861(95)90922-O.
18. Glaeser, R. M.; Taylor, K. A. Radiation damage relative to transmission electron microscopy of biological specimens at low temperature: a review. *Journal of microscopy* **1978,** 112 (1), 127-38.
19. Egerton, R. F. Control of radiation damage in the TEM. *Ultramicroscopy* **2013,** 127, 100-8 DOI: 10.1016/j.ultramic.2012.07.006.
20. Li, X. M.; Mooney, P.; Zheng, S.; Booth, C. R.; Braunfeld, M. B.; Gubbens, S.; Agard, D. A.; Cheng, Y. F. Electron counting and beam-induced motion correction enable near-atomic-resolution single-particle cryo-EM. *Nat Methods* **2013,** 10 (6), 584-+ DOI: 10.1038/nmeth.2472.

21. Kuhlbrandt, W. The Resolution Revolution. *Science* **2014,** 343 (6178), 1443-1444 DOI: 10.1126/science.1251652.
22. Cheng, Y. F. Single-Particle Cryo-EM at Crystallographic Resolution. *Cell* **2015,** 161 (3), 450-457 DOI: 10.1016/j.cell.2015.03.049.
23. Scheres, S. H. RELION: implementation of a Bayesian approach to cryo-EM structure determination. *Journal of structural biology* **2012,** 180 (3), 519-30 DOI: 10.1016/j.jsb.2012.09.006.
24. Zheng, S. Q.; Palovcak, E.; Armache, J. P.; Verba, K. A.; Cheng, Y. F.; Agard, D. A. MotionCor2: anisotropic correction of beam-induced motion for improved cryo-electron microscopy. *Nat Methods* **2017,** 14 (4), 331-332 DOI: 10.1038/nmeth.4193.
25. Fischer, N.; Neumann, P.; Konevega, A. L.; Bock, L. V.; Ficner, R.; Rodnina, M. V.; Stark, H. Structure of the E. coli ribosome-EF-Tu complex at < 3 angstrom resolution by C-s-corrected cryo-EM. *Nature* **2015,** 520 (7548), 567-+ DOI: 10.1038/nature14275.
26. Henderson, R.; Baldwin, J. M.; Downing, K. H.; Lepault, J.; Zemlin, F. Structure of Purple Membrane from Halobacterium-Halobium - Recording, Measurement and Evaluation of Electron-Micrographs at 3.5 a Resolution. *Ultramicroscopy* **1986,** 19 (2), 147-178 DOI: Doi 10.1016/0304-3991(86)90203-2.
27. Chiu, P. L.; Li, X. M.; Li, Z. L.; Beckett, B.; Brilot, A. F.; Grigorieff, N.; Agard, D. A.; Cheng, Y. F.; Walz, T. Evaluation of super-resolution performance of the K2 electron-counting camera using 2D crystals of aquaporin-O. *Journal of structural biology* **2015,** 192 (2), 163-173 DOI: 10.1016/j.jsb.2015.08.015.
28. Sun, J.; Jiang, X.; Lund, R.; Downing, K. H.; Balsara, N. P.; Zuckermann, R. N. Self-assembly of crystalline nanotubes from monodisperse amphiphilic diblock copolypeptoid tiles. *P Natl Acad Sci USA* **2016,** 113 (15), 3954-3959 DOI: 10.1073/pnas.1517169113.
29. Gipson, B.; Zeng, X.; Zhang, Z. Y.; Stahlberg, H. 2dx--user-friendly image processing for 2D crystals. *Journal of structural biology* **2007,** 157 (1), 64-72 DOI: 10.1016/j.jsb.2006.07.020.
30. Rohou, A.; Grigorieff, N. CTFFIND4: Fast and accurate defocus estimation from electron micrographs. *Journal of structural biology* **2015,** 192 (2), 216-21 DOI: 10.1016/j.jsb.2015.08.008.

For Table of Contents use only